

Bayesian inference for high-dimensional discrete-time epidemic models: spatial dynamics of the UK COVID-19 outbreak

Chris P Jewell

Department of Mathematics and Statistics, Lancaster University, Lancaster, LA1 4YW, U.K.

E-mail: c.jewell@lancaster.ac.uk

Alison C Hale

Department of Mathematics and Statistics, Lancaster University, Lancaster, LA1 4YW, U.K.

Barry S. Rowlingson

Lancaster Medical School, Lancaster University, Lancaster, LA1 4YW, UK

Christopher Suter

Google Research

Jonathan M. Read

Lancaster Medical School, Lancaster University, Lancaster, LA1 4YW, UK

Gareth Roberts

Department of Statistics, University of Warwick, Coventry, CV4 7AL, U.K.

Summary. Stochastic epidemic models which incorporate interactions between space and human mobility are a key tool to inform prioritisation of outbreak control to appropriate locations. However, methods for fitting such models to national-level population data are currently unfit for purpose due to the difficulty of marginalising over high-dimensional, highly-correlated censored epidemiological event data. Here we propose a new Bayesian MCMC approach to inference on a spatially-explicit stochastic SEIR meta-population model, using a suite of novel model-informed Metropolis-Hastings samplers. We apply this method to UK COVID-19 case data, showing real-time spatial results that were used to inform UK policy during the pandemic.

Keywords: Stochastic epidemic model, spatial epidemic, COVID-19, Bayesian statistics, MCMC

1. Introduction

During the COVID-19 pandemic, accurate situational awareness and the ability to project case numbers forward in time was an important aspect of adaptive infection control policy. In the UK, as elsewhere, the epidemic was characterised by dramatically fluctuating case numbers over space and time, with population behaviour interacting with pathogen transmission to create a complex and highly-variable disease landscape.

Understanding this variability in case numbers became an important aspect of epidemic management, and quantitative modelling of the drivers of infection transmission enabled metrics such as the time-varying reproduction number, intrinsic growth rate, and the impact of intervention strategies to be estimated.

Epidemic dynamics are largely driven by the characteristics of the population at risk: the behavioural determinants of how individuals interact, socioeconomics and spatially-varying population density and environment in which people live (Grenfell et al., 2002). In particular, the spatial distribution and mobility of a population has a marked impact on the pattern of disease transmission, and understanding how epidemic behaviour responds to individuals' mobility is a key aspect of outbreak control (Keeling et al., 2001). At both a local and national level, infectious disease transmission may be assumed to be facilitated by individual-to-individual contact, and therefore understanding how contact behaviour spreads infection is central in designing successful control interventions whilst minimising public disturbance (Keeling and Eames, 2005).

Stochastic individual-level state-transition models of epidemics have been extensively used to study the effects of spatial population structure on epidemic spread (Keeling et al., 2001). They are a special case of the more general class of state-transition processes, which consider individuals as transitioning between a number of discrete, mutually-exclusive states reflecting the expected natural history of infection according to a stochastic process (Bartlett, 1964). For example, the classic SEIR model (Figure 1) assumes individuals begin as *susceptible* to infection, and transition sequentially to *exposed* (i.e. infected but not yet infectious), *infectious*, and finally *removed* (i.e. dead or recovered with immunity from further infection). Of particular interest is the infection rate, or hazard rate of transitioning from *susceptible* to *exposed*, which given a suitable model can provide valuable insights into how interactions between individuals modulate the propensity for disease transmission as a function of spatial separation, as well as how individual-level covariates affect disease susceptibility and infectivity (e.g. Jewell et al., 2009; Smieszek et al., 2011). These models are particularly popular due to their interpretability and compatibility with decision-making questions (e.g. Tildesley et al., 2006; Palomo-Briones et al., 2022).

Though powerful, individual-level models are computationally intensive, with fast forward simulation and inference methods requiring model-specific optimisations, and inference methods requiring application-specific approximations to allow fast computation of likelihood functions (Deardon et al., 2010; Brand et al., 2015; Sellman et al., 2018; Probert et al., 2018). Additionally, whilst such methods have been used successfully for population sizes up to approximately 200,000 (commonly suiting livestock disease applications as in Probert et al. (2018)), individual-level covariate data is rarely available to support modelling at the individual level for national and international human populations. In such situations, the population may be stratified by group-level covariates of interest. Stratification by space leads to the metapopulation model, in which individuals are aggregated into a number of discrete spatial units, with individuals within a spatial unit sharing a set of common covariates (Levins, 1969). The exchangability of individuals within each metapopulation hence offers performance gains in both computation time and storage.

For models with modest numbers of metapopulations (low-dimensional models), a

popular approach is to represent the state transition model as a system of ordinary differential equations, using a continuous mean-field approximation to the discrete space of numbers of individuals transiting through the state-transition graph (e.g. Lipshtat et al., 2021). However, increasing numbers of metapopulations (high-dimensional models) divides the population into smaller units, such that the continuous state-space approximation of the ODE system fails. In this case, a stochastic implementation is required that captures the random nature of infection transmission among small numbers of individuals within the metapopulation. Whilst metapopulation models can be implemented as a continuous time-inhomogeneous Poisson process (e.g. Minh et al., 2011), a more computationally convenient setup is the discrete-time “chain-binomial” model (Becker, 1981). This has the additional computational performance advantage that complexity may be controlled by packaging transition events into time-quanta, rather than having to compute for each individual transition event in continuous time (Diekmann et al., 2021).

In a real-time outbreak response context, the utility of epidemic models is maximised through principled parameter inference, providing important policy information through improved situational awareness and forecasting of the ongoing epidemic in space and time (Jewell et al., 2009; Birrell et al., 2021). Given complete epidemic information, i.e. the epidemiological states and transition times for each individual over the course of the epidemic, the likelihood function of a given state-transition model is tractable and amenable to conventional inference methods. However, in all real-world situations inference is complicated by the inability to directly observe individuals’ epidemiological states, or certain transition events. For example, whereas the times of individual symptom onset or recovery might be well-recorded, infection events are typically unobserved (Chapman et al., 2018). The demands on inference methods for real-time epidemic model fitting therefore present a considerable statistical challenge: not only must the method be rapid in its own right, but must *also* be flexible enough to marginalise over potentially many censored transition events and epidemiological states (Swallow et al., 2022).

In this paper we shall adopt a Bayesian approach to inference for stochastic metapopulation models, as demonstrated by our COVID-19 application. This has many advantages: it provides a principled and coherent calculus for the measurement of uncertainty both in parameters and predictions of future epidemic scenarios; it gives a natural way of taking into account missing and censored data using data augmentation; it provides a natural framework for experts to input knowledge to inform inference (via prior elicitation); and finally its implementation is facilitated through powerful MCMC techniques. That being said, MCMC methods are often seriously challenged by spatial applications at scale due to the strong correlations inherently present within such models. For individual-level models, data-augmentation methodology has become state-of-the-art for unbiased parameter estimation, allowing efficient marginalisation over the censored data (Neal and Roberts, 2004; Jewell et al., 2009; Probert et al., 2018; Chapman et al., 2018). However, these methods scale poorly to large population sizes, and are therefore unsuitable for the COVID-19 epidemic at hand. Whilst particle filter methods are beginning to show promise for fitting larger-scale epidemic models, they are inherently constrained by poor performance as the dimensionality of the population stratification

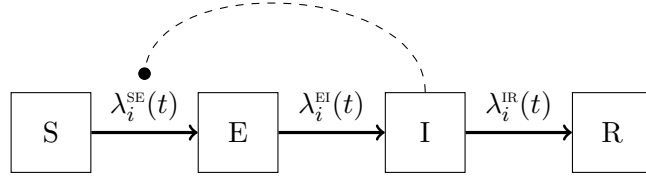


Fig. 1. SEIR model showing states (boxes), transitions (arrows), and associated transition rates.

increases (Rimella et al., 2023). Inspired by existing data-augmentation methodology, we therefore develop a novel MCMC method suited to metapopulation models, and which are amenable to rapid implementation through efficient multi-core computing. Our innovations allow us to analyse national-scale outbreaks in a timely manner, capturing spatiotemporal dependence between disease prevalence and incidence. This then provides estimates of quantities such as the degree of interaction between population strata and reproduction number, and predictions of the ongoing disease trajectory.

Between May 2020 and March 2022, the modelling approach to the UK’s COVID-19 outbreak we describe in this paper was used to provide information to the UK government, via the Scientific Pandemic Influenza Group on Modelling, Operational sub-group (SPI-M-O) of the Scientific Advisory Group on Emergencies (SAGE).

1.1. Spatial COVID-19 cases in the UK

Data on the daily number of new cases of COVID-19 in each of 382 Local Authority Districts (LADs) in the UK is available from the UK Government Coronavirus website (Public Health England, 2020, 2021). This dataset contains the number of people y_{it} who submitted a positive test sample for COVID-19 on day t in LAD i , where a positive test is defined as positive by PCR or by LFD followed by confirmatory PCR. In practice we further spatially aggregated Cornwall and the Isles of Scilly due to the latter’s small population size, and likewise City of London and City of Westminster for a total of 380 discrete spatial units.

From May 2020 until March 2022, we ran our analysis daily on an 84 day sliding window. In practice, for an analysis on day t , we used data in the interval $[t - 88, t - 4)$, discarding the latest 4 days’ worth of data due to significant recording lag. For the purposes of exposition in this paper, however, we restrict our results to the 84 day window between 7th June 2021 and 31th August 2021 inclusive. This covered the emergence of the SARS-CoV-2 Delta (B.1.617.2) strain, and was after social distancing regulations had been relaxed. Figure 2 shows the daily case counts and overall incidence map for this period.

Connectivity between LADs was informed by freely available Census 2011 commuting volume data aggregated from Middle Super Output Area (MSOA) onto our 380 LAD-based spatial units. These data provide a matrix G with g_{ij} $i, j = 1, \dots, 380$ being the number of journeys made from “residence” j to “workplace” i . G is non-symmetric, reflecting commuting behaviour rather than the reciprocity of disease transmission. We therefore calculated a symmetric matrix $C = G + G^T$ of the daily number of journeys

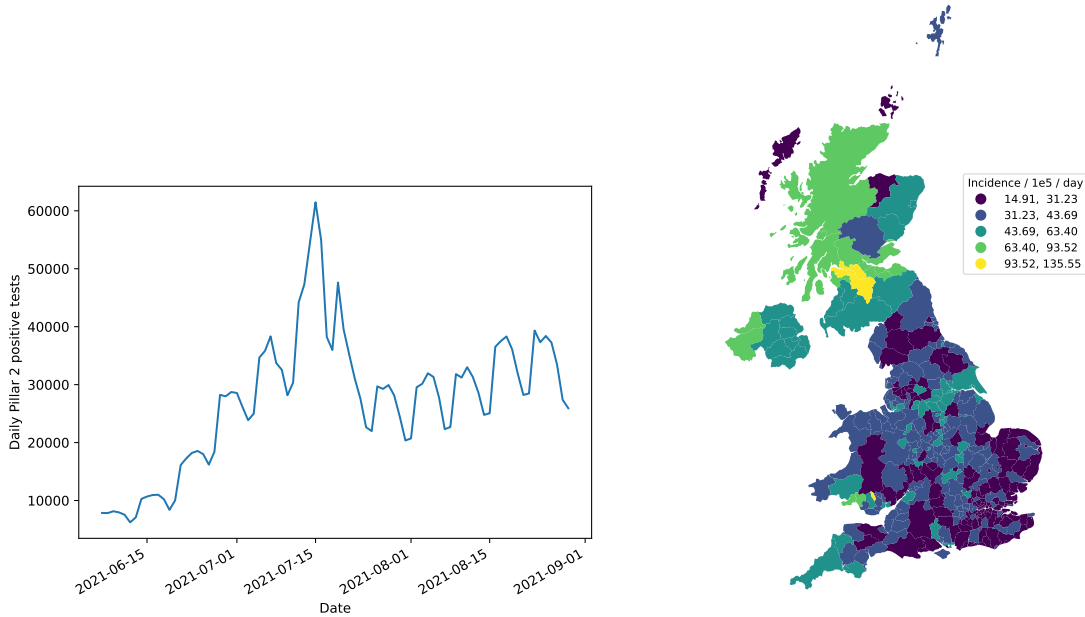


Fig. 2. Cases of COVID-19 in the UK, as determined by daily numbers of Pillar 2 positive tests. Left: COVID-19 daily case counts between 7th June and 29th August 2021 inclusive, showing marked weekly variation and long-term drift; Right: Spatial distribution of COVID-19 cases as of 29th August 2021, expressed as incidence per 100000 people per day. Concentrations of high incidence are observed in Scotland, Northern Ireland, and Wales.

between each LAD assuming that commuters return to their residence each day, and go from their residence to their workplace and back at most once per day. We also set $C_{ii} = 0$, for all i as within-LAD infection transmissibility is delegated to another part of our model (Section 2).

Finally, we introduce LAD-level population estimates and LAD polygon area to inform how transmission varies with population size. In all datasets, two pairs of LADs (Cornwall and Scilly, and City of Westminster and City of London) are merged to allow mapping of MSOAs onto LADs resulting in data geolocated to 380 spatial units.

2. Model

In the following sections, we construct a model to represent the epidemic in terms of the number of individuals testing positive on each day $t = 0, \dots, T - 1$ within spatial unit $i = 1, \dots, M$ defined by UK Local Authority Districts. Since our motivation is to measure quantities such as the degree of disease transmission between spatial units and reproduction number, and predict the ongoing disease trajectory, we are interested in capturing spatiotemporal dependence between disease prevalence and incidence.

Below, we first describe a linear state transition model that captures the natural history of the COVID-19 disease progression per individual, accounting for segregation

of the population at risk into discrete spatial units. We then describe how this model is set up as a discrete time Markov process, establishing a notation allowing us to describe our inference methodology in the next section.

2.1. State transition model

Within each spatial unit, we model the COVID-19 epidemic by assuming that at any time t individuals exist in one of 4 mutually exclusive disease states: susceptible, exposed (infected but not yet infectious), infectious, and removed which we denote by S, E, I, and R respectively. We assume that individuals progress sequentially between the disease states, such that the allowed transitions are [SE], [EI], and [IR] as shown in Figure 1. Each transition is associated with a hazard rate, $\lambda_i^{\text{SE}}(t)$, $\lambda_i^{\text{EI}}(t)$, and $\lambda_i^{\text{IR}}(t)$ respectively giving the transition rate between states for a single individual, and allowing us flexibility to specify how they evolve over space and time.

2.1.1. Infection rate

The infection hazard rate $\lambda_i^{\text{SE}}(t)$ is space- and time-dependent, parameterised as a product of a log-linear term describing the susceptibility of an individual in i to infection, and a function of infectious challenge assuming homogeneous mixing of individuals within each spatial unit i and mixing due to commuting flows between i and all other spatial units $j \neq i$. We scale the hazard rate by the local population size n_i following the usual assumption of frequency-dependent disease transmission. Thus

$$\lambda_i^{\text{SE}}(t) = \frac{\exp(u_t + s_i)}{n_i} \left[x_{it}^I + \psi \sum_{j \neq i} \frac{c_{ij} x_{jt}^I}{n_j} \right]$$

where u_t is a temporally-correlated random effect, s_i a spatially-correlated random effect, x_{it}^I is the number of infectious individuals in i at time t (see below), and c_{ij} represents the commuting flow to spatial unit i from spatial unit j . The coefficient ψ is assumed unknown and is to be estimated given the data.

Due to the considerable variability in the infection dynamics of the COVID-19 outbreak we assume a random walk for the temporally-correlated random effect \mathbf{u} , such that

$$u_t = \begin{cases} \alpha_0 & \text{if } t = 0 \\ u_{t-1} + \alpha_t & \text{if } t > 0 \end{cases}$$

with

$$\begin{aligned} \alpha_0 &\sim \text{Normal}(0, 10) \\ \alpha_t &\stackrel{\text{iid}}{\sim} \text{Normal}(0, \sigma_u^2), \quad t > 0 \end{aligned}$$

and $\sigma_u = 0.005$ chosen heuristically.

Furthermore, we assume that the spatially-correlated random effect follows a Conditional Autoregressive (CAR) process with joint distribution

$$\mathbf{s} \sim \text{MVN}(\mathbf{0}, \Sigma).$$

The covariance matrix Σ is specified in terms of an adjacency matrix W with elements $(W)_{ij} = 1 \iff i \sim j$ and 0 otherwise, and a diagonal matrix D_w with element $(D_w)_{ii} = W \cdot \mathbf{1}$ (i.e. the number of spatial units neighbouring i) such that

$$\Sigma = \sigma_s^2 (D_w - \rho W)^{-1}$$

with σ_s an unknown parameter and correlation parameter $\rho = 0.25$ chosen heuristically to give a smooth posterior surface across LADs in an effort to improve reliability of model fitting by keeping the number of free parameters to a minimum. We note that in a less operational context, a Besag-York-Mollié model might be preferred, though it would require the development of more complex and bespoke MCMC methodology to fit in the presence of latent event times.

The following prior distributions are imposed on the remaining free parameters

$$\begin{aligned} \psi &\sim \text{Gamma}(0, 100) \\ \sigma_s &\sim \text{HalfNormal}(0.1) \end{aligned}$$

2.1.2. Latent and infectious periods

The latent period (sojourn in E) and infectious period (sojourn in I) are parameterised through the transition rates $\lambda_i^{\text{EI}}(t)$ and $\lambda_i^{\text{IR}}(t)$. Evidence from the literature suggests a mean latent period of 5 - 7 days (Quesada et al., 2021), with a mean infectious period of 5 days starting 2 days before the onset of symptoms (Tian et al., 2020). In the context of our model, we therefore assume

$$\lambda_i^{\text{EI}}(t) = 0.25$$

giving an *effective* 4 day mean latent period irrespective of time and space. For the infectious period, we assume

$$\lambda_i^{\text{IR}}(t) = e^{\gamma_0 + \gamma_1 g_t}$$

irrespective of space, where $\gamma_0 = \log 0.25$ is the (known) mean log hazard rate for removal ([IR]) events, γ_1 the (unknown) log hazard ratio for being removed on a weekday versus the weekend, and

$$g_t = \begin{cases} -\frac{2}{7} & \text{if } t \in \{\text{mon}, \dots, \text{fri}\} \\ \frac{5}{7} & \text{otherwise} \end{cases}$$

to stabilise the inference. We assume that *a priori* $\gamma_1 \sim \text{Normal}(0, 100)$.

2.2. Discrete-time Markov chain implementation

In this section, we implement the SEIR state transition model described in Section 2.1 as a discrete-time stochastic process, more specifically a discrete-time finite state-space Markov chain using the so-called ‘‘chain binomial’’ setup (e.g. Becker, 1981).

For timepoint t and spatial unit i , let x_{it}^q represent the number of individuals resident in state $q \in \{\text{S}, \text{E}, \text{I}, \text{R}\}$, and y_{it}^{qr} for transition $[qr] \in \{[\text{SE}], [\text{EI}], [\text{IR}]\}$ represent the

number of transitions occurring between each state. Given an initial state \mathbf{x}_0 , we evolve the epidemic by iterating

$$y_{it}^{qr} \sim \text{Binomial}(x_{it}^q, p_i^{qr}(t)), \quad [qr] \in \{[SE], [EI], [IR]\} \quad (5)$$

and

$$\begin{aligned} x_{i,t+1}^S &= x_{it}^S - y_{it}^{SE} \\ x_{i,t+1}^E &= x_{it}^E + y_{it}^{SE} - y_{it}^{EI} \\ x_{i,t+1}^I &= x_{it}^I + y_{it}^{EI} - y_{it}^{IR} \\ x_{i,t+1}^R &= x_{it}^R + y_{it}^{IR} \end{aligned} \quad (6)$$

where the transition probabilities $p_i^{qr}(t) = 1 - e^{-\lambda_i^{qr}(t)\delta t}$ are assumed constant throughout each timestep of size δt .

Considering (5) as the data generating model, a realisation of the Markov chain results in the $T \times M$ state matrices \mathbf{x}^q and event matrices \mathbf{y}^{qr} giving the state of the Markov chain at each timepoint and transition events responsible for evolving the state.

3. Inference

In order to fit our model to the spatial timeseries of positive COVID-19 tests across the UK, we make the assumption that the occurrence of a positive test is equivalent to observing a [IR] event. Furthermore, since the [SE] or [EI] events are censored, we adopt the conventional statistical notation $z_{it}^{SE} = y_{it}^{SE}$ and $z_{it}^{EI} = y_{it}^{EI}$ to denote the presence of censored data \mathbf{z} .

Given the data generating model given in Equations (5) and (6), and conditional on unknown parameter vector $\boldsymbol{\theta} = \{\psi, \sigma_s, \gamma_1, \boldsymbol{\alpha}, \mathbf{s}\}$ and initial conditions \mathbf{x}_0 , the log likelihood of observing transitions \mathbf{y} , censored transitions \mathbf{z} , and states $\mathbf{x}_{1:T}$ given a set of initial conditions \mathbf{x}_0 and $\boldsymbol{\theta}$ is

$$\begin{aligned} \ell(\mathbf{y}, \mathbf{z}, \mathbf{x}|\mathbf{x}_0, \boldsymbol{\theta}) &= \sum_{t=0}^{T-1} \sum_{i=1}^M [z_{it}^{SE} \log p_i^{SE}(t) + (x_{it}^I - z_{it}^{SE}) \log(1 - p_i^{SE}(t)) + \\ &\quad z_{it}^{EI} \log p_i^{EI}(t) + (x_{it}^E - z_{it}^{EI}) \log(1 - p_i^{EI}(t)) + \\ &\quad y_{it}^{IR} \log p_i^{IR}(t) + (x_{it}^I - y_{it}^{IR}) \log(1 - p_i^{IR}(t))] \end{aligned}$$

We estimate the joint posterior of the parameters and missing data $\pi(\boldsymbol{\theta}, \mathbf{z}|\mathbf{y}, \mathbf{x}_0)$ by using a Metropolis-within-Gibbs MCMC scheme in which we draw alternately from $\pi(\boldsymbol{\theta}|\mathbf{z}, \mathbf{y}, \mathbf{x}_0)$ by adaptive Hamiltonian Monte Carlo, and $\pi(\mathbf{z}|\boldsymbol{\theta}, \mathbf{y}, \mathbf{x}_0)$ using a discrete-space Metropolis Hastings step. A high-level description of our approach is shown in Algorithm 1.

The adaptive Hamiltonian Monte Carlo algorithm for drawing from $\pi(\boldsymbol{\theta}|\mathbf{z}, \mathbf{y}, \mathbf{x}_0)$ is well-described elsewhere (see for example Carpenter et al., 2017), and therefore in the following sections we focus on describing the methodology for drawing from $\pi(\mathbf{z}|\boldsymbol{\theta}, \mathbf{y}, \mathbf{x}_0)$ and $\pi(\mathbf{x}_0, \mathbf{z}|\boldsymbol{\theta}, \mathbf{y})$.


```

Initialise  $\boldsymbol{\theta}^{(0)}, \mathbf{z}^{(0)}$ 
for  $k$  in  $1, \dots, K$  do
  Update  $\boldsymbol{\theta}$  by HMC
  for  $l$  in  $1, \dots, L$  do
    Update partially-censored events in  $\mathbf{z}^{\text{SE}}$ 
    Update partially-censored events in  $\mathbf{z}^{\text{EI}}$ 
    Update occult events in  $\mathbf{z}^{\text{SE}}$ 
    Update occult events in  $\mathbf{z}^{\text{EI}}$ 
    Update initial conditions  $\mathbf{x}_0$  for events  $\mathbf{z}^{\text{SE}}$ 
    Update initial conditions  $\mathbf{x}_0$  for events  $\mathbf{z}^{\text{EI}}$ 

```

Algorithm 1: Overall Metropolis-within-Gibbs MCMC algorithm for sampling from the joint posterior.

3.1. Drawing samples from $\pi(\mathbf{z}|\boldsymbol{\theta}, \mathbf{y}, \mathbf{x}_0)$

In this section we describe the discrete-space Metropolis-Hastings algorithms used to draw samples from the conditional posterior of the censored events and initial conditions given state transition parameters and data, $\pi(\mathbf{z}, \mathbf{x}_0|\boldsymbol{\theta}, \mathbf{y})$. The approach follows the principles for data-augmentation in individual level models (see for example Jewell et al., 2009), which involves two separate Metropolis-Hastings kernels to explore the space of partially-censored and fully-censored events respectively. Unlike in the continuous-time setting, for our discrete model we also introduce a third Metropolis-Hastings kernel which explores the initial conditions space.

In the context of our model, the challenge to successful updating of censored event times is to create a proposal mechanism that respects the constraint that $x_{it}^q \geq 0$ for all $q \in \{\text{S}, \text{E}, \text{I}, \text{R}\}$ and $t = 0, \dots, T - 1$ and $i = 1, \dots, M$.

3.1.1. Updating partially-censored events

The proposed Metropolis Hastings kernel operates on a $M \times T$ censored event matrix \mathbf{z}^{qr} , $[qr] \in \{\text{SE}, \text{EI}\}$. The algorithm proceeds by proposing to move a number of events w from z_{it}^{qr} to z_{it+d}^{qr} where we draw

$$\begin{aligned}
i, t &\sim \text{Discrete}(i, t : z_{it}^{qr} > 0) \\
d &\sim \text{Discrete}(0 \vee t - d_{\max}, \dots, -1, 1, \dots, T \wedge t + d_{\max}) \\
w &\sim \text{Discrete}(1, \dots, B_1(z_{it}^{qr}))
\end{aligned} \tag{7}$$

where $d_{\max} > 0$ is a tuning constant, and with bounding function

$$B_1(z_{it}^{qr}) = z_{it}^{qr} \wedge w_{\max} \wedge \begin{cases} \min(x_{it}^r, \dots, x_{i,t+d-1}^r) & \text{if } d > 0 \\ \min(x_{i,t-d}^q, \dots, x_{t-1}^q) & \text{if } d < 0 \end{cases}$$

where $w_{\max} > 0$ is also a tuning constant.

We then propose

$$\begin{aligned} z_{it}^{qr*} &= z_{it}^{qr} - w \\ z_{t+\delta,i}^{qr*} &= z_{t+\delta}^{qr} + w \end{aligned}$$

and accept the proposal with probability

$$\alpha(\mathbf{z}^{qr}, \mathbf{z}^{qr*}) = \frac{\pi(\mathbf{z}^{qr*} | \boldsymbol{\theta}, \mathbf{y}, \mathbf{x}_0)}{\pi(\mathbf{z}^{qr} | \boldsymbol{\theta}, \mathbf{y}, \mathbf{x}_0)} \cdot \frac{\text{nnz}(\mathbf{z}^{qr*}) B_1(z_{it}^{qr*}; \mathbf{x}^*)}{\text{nnz}(\mathbf{z}^{qr}) B_1(z_{it}^{qr}; \mathbf{x})} \wedge 1$$

where $\text{nnz}(\mathbf{z}^{qr})$ denotes the number of non-zero elements in \mathbf{z}^{qr} .

3.1.2. Updating occult events

To explore the space of occult events, we again operate on $M \times T$ censored event matrices \mathbf{z}^{qr} , $[\text{qr}] \in \{[\text{SE}], [\text{EI}]\}$, proposing to add or delete a number of events to randomly chosen elements. In our model, occult events are overwhelmingly likely to occur close to the end of the analysis time-window, and so we limit our choice of elements to those in the last 21 days of the timeseries.

To add events, we choose an element z_{it}^{qr} to update via

$$\begin{aligned} i &\sim \text{Discrete}(1, \dots, M) \\ t &\sim \text{Discrete}(T - 21, \dots, T) \end{aligned}$$

and propose to add v events by

$$v \sim \text{Discrete}(1, \dots, B_2(\mathbf{z}_{it}^{qr})),$$

where bounding function

$$B_2(z_{it}^{qr}) = v_{\max} \wedge \min(x_{it}^q, \dots, x_{iT}^q)$$

with v_{\max} a tuning constant.

We then update $z_{it}^{qr*} = z_{it}^{qr} + v$, and accept the proposal with probability

$$\alpha(\mathbf{z}^{qr}, \mathbf{z}^{qr*}) = \frac{\pi(\mathbf{z}^{qr*} | \boldsymbol{\theta}, \mathbf{y}, \mathbf{x}_0)}{\pi(\mathbf{z}^{qr} | \boldsymbol{\theta}, \mathbf{y}, \mathbf{x}_0)} \cdot \frac{21MB_2(\mathbf{z}^{qr})}{\text{nnz}(\mathbf{z}^{qr*}) B_3(\mathbf{z}^{qr*})} \wedge 1$$

with $B_3(\mathbf{z}^{qr*})$ defined below.

To delete events, we restrict our choice of i and t to positive elements of \mathbf{z}^{qr} as in Equation (7), and propose

$$\begin{aligned} i, t &\sim \text{Discrete}(i, t : z_{it}^{qr} > 0, t \geq T - 21) \\ v &\sim \text{Discrete}(1, \dots, B_3(z_{it}^{qr}; \mathbf{x})) \end{aligned}$$

where bounding function

$$B_3(z_{it}^{qr}) = z_{it}^{qr} \wedge v_{\max} \wedge \min(x_{it}^r, \dots, x_{iT}^r).$$

We then accept the proposal $z_{it}^{qr*} = z_{it}^{qr} - v$ with probability

$$\alpha(\mathbf{z}^{qr}, \mathbf{z}^{qr*}) = \frac{\pi(\mathbf{z}^{qr*} | \boldsymbol{\theta}, \mathbf{y}, \mathbf{x}_0)}{\pi(\mathbf{z}^{qr} | \boldsymbol{\theta}, \mathbf{y}, \mathbf{x}_0)} \cdot \frac{\text{nnz}(\mathbf{z}^{qr}) B_3(\mathbf{z}^{qr})}{21MB_2(\mathbf{z}^{qr*})} \wedge 1.$$

3.1.3. Updating initial conditions

In the third data-augmentation kernel, we update the initial conditions matrix \mathbf{x}_0 . Given that we assume a closed population, such that $\mathbf{x}^S + \mathbf{x}^E + \mathbf{x}^I + \mathbf{x}^R = \mathbf{N}$ the size vector of the population, we have two options for updating \mathbf{x}_0 . The first would be to swap individuals between pairs of adjacent epidemiological states. However, since \mathbf{x}_0 is a *posteriori* conditional on the events \mathbf{z} , the small conditional variance $Var(\mathbf{x}_0|\mathbf{z}, \mathbf{y}, \boldsymbol{\theta})$ results in slow exploration of the censored data space. Instead, we employ a *joint* update of \mathbf{x}_0 and \mathbf{z} in which we consider a set of left-censored events occurring prior to timepoint $t = 0$ that have given rise to \mathbf{x}_0 .

For a given transition [qr], we begin as before by choosing an element z_{it}^{qr} to update

$$\begin{aligned} i &\sim \text{Discrete}(1, \dots, M) \\ t &\sim \text{Discrete}(0, \dots, 6). \end{aligned}$$

noting that we restrict the choice of t to a window $[0, 7)$ at the beginning of the epidemic – this helps to reduce the possible dimensionality of the discrete random walk, since it is unlikely that left-censored events could be moved to later timepoints without large changes in the posterior leading to a rejected move.

We now choose to either move events forwards ($d = 1$) or backwards ($d = -1$) in time with equal probability such that

$$d \sim \text{Discrete}(-1, 1)$$

and a number of events to move such that

$$h \sim \text{Discrete}(1, \dots, B_4(\mathbf{x}_0))$$

with

$$B_4(\mathbf{x}_0) = h_{\max} \wedge \begin{cases} z_{it}^{qr} \wedge \min(x_{i1}^q, \dots, x_{it}^q) & \text{if } d = -1 \\ \min(x_{i0}^r, \dots, x_{it-1}^r) & \text{if } d = 1 \end{cases}$$

and where $h_{\max} > 1$ is a tuning constant. We then let

$$\begin{aligned} x_{i0}^{q*} &= x_{i0}^q + dh \\ x_{i0}^{r*} &= x_{i0}^r - dh \\ z_{it}^{qr*} &= z_{it}^{qr} + dh \end{aligned}$$

and accept the proposal with

$$\alpha(\mathbf{x}_0, \mathbf{z}, \mathbf{x}_0^*, \mathbf{z}^*) = \frac{\pi(\mathbf{x}_0^*, \mathbf{z}^*|\mathbf{y}, \boldsymbol{\theta})}{\pi(\mathbf{x}_0, \mathbf{z}|\mathbf{y}, \boldsymbol{\theta})} \cdot \frac{B_4(\mathbf{x}_0^*)}{B_4(\mathbf{x}_0)} \wedge 1.$$

We note that if $B_4 = 0$, then $f_k(h) = 0 \forall h$ in Equation 3.1.3 and the move will be rejected.

3.2. Definition of R_t

We define an approximate stratified temporal reproduction number R_{jt} as the expected number of further individuals that an individual in stratum j will go on to infect given

the state at time t . We define this by first considering the pairwise force of infection defined by \mathbf{K} exerted by an individual in j on a susceptible individual in i such that

$$\mathbf{R}_t \approx \frac{1 - \exp\left(-(\mathbf{X}_{\cdot t}^s)^T \cdot \mathbf{K}\right)}{1 - \exp(-\gamma_0)}$$

We remark that this is an approximation since both $\mathbf{X}_{\cdot t}^s$ (and therefore $\lambda^{\text{SE}}(t)$) is assumed constant over the course of an individual's infectious period.

3.3. Software implementation

The model and sampler code were implemented in Python 3.8 using TensorFlow and TensorFlow Probability computational and probabilistic programming libraries for GPU acceleration (Abadi et al., 2015; Dillon et al., 2017). The Python code implementing this analysis is freely available under the MIT license at <https://gitlab.com/chicas-covid19/covid19uk>, with the Version 1.0 snapshot available at <https://doi.org/10.5281/zenodo.7715657>.

4. Sampler optimisation

Before addressing the real-world application, we demonstrate that the discrete-space samplers described above are optimised at the conventional accept/reject ratio of 0.23. Here we provide results for tuning m , the number of metapopulations and w , the number of events for the partially-observed event time moves described in Section 3.1.1, as applied to the [SE] and [EI] transitions respectively.

We first define the mean squared jumping distance to be

$$\text{MSJD} = \frac{1}{K} \sum_{k=1}^K \sum_{i,t,s} \left(x_{it}^{s(k)} - x_{it}^{s(k-1)}\right)^2.$$

We then run the partially-observed event time sampler separately for the [SE] and [EI] transitions respectively, considering all other censored data and parameters fixed at values taken from a randomly-chosen iteration of the converged MCMC chain described in Section 5. For each transition, we run the sampler for $(m, x_{max}) \in \{m : 1, \dots, 10\} \times \{x_{max} : 1, \dots, 100\}$ with m and x_{max} as defined in Section 3.

For each transition and (m, x_{max}) tuple, we plot the MSJD against the acceptance ratio in Figure 3. This confirms that the MSJD is maximised at an acceptance ratio of approximately 0.234 irrespective of the transition. However, the way in which (m, x_{max}) affects the MSJD differs depending on the transition selected. Moreover, we observe that the total number of events moved across all selected metapopulations is conserved, such that as long as $m x_{max} \approx 30$ we achieve the maximum MSJD.

5. Application to the UK COVID-19 epidemic

In this section we apply the model described in Section 2 to the UK COVID-19 spatial case timeseries shown in Section 1.1. The MCMC algorithms were run for $k = 40000$

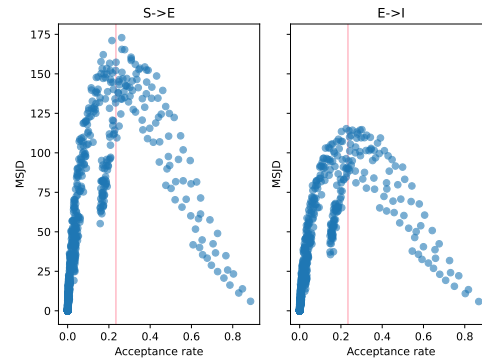


Fig. 3. Mean squared jumping distance versus acceptance probability for the [SE] (left) and [EI] (right) optimisation studies respectively (Section 4). Blue dots represent each combination of m and x_{max} , and red vertical line indicates theoretically optimal acceptance rate.

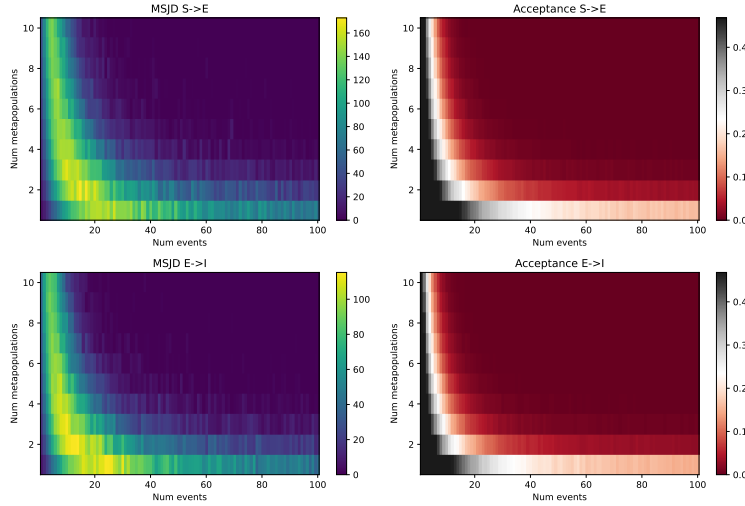


Fig. 4. Mean squared jumping distance (left) and Metropolis Hastings acceptance probability (right) for the *move* algorithm for both the [SE] (top) and [EI] (bottom) transitions.

Table 1. Tuning constants used for MCMC algorithm to fit the spatial stochastic meta-population model to COVID-19 case time-series data.

Transition	Update	Tuning constant	Value
[SE]	Partially-censored	d_{max}	84
		w_{max}	22
	Fully-censored	v_{max}	20
	Initial conditions	h_{max}	19
[EI]	Partially-censored	d_{max}	84
		w_{max}	18
	Fully-censored	v_{max}	20
	Initial conditions	h_{max}	17

iterations, with $l = 380$ censored event updates per iteration (Algorithm 1) with tuning constants as in Table 1. Three independent MCMC algorithms were run, initialising each Markov chain using a random draw from the prior distribution, and discarding the first 10000 iterations for any calculated quantities (R_t , riskmaps, and predictive distributions).

Traceplots of the scalar quantities $\exp(\alpha_0)$, $\exp(\gamma_1)$, ψ are shown in Figure 5, superimposing the three independent chains and calculating the Brookes-Gelman-Rubin statistics (\hat{R} , not to be confused with the time-varying reproduction number R_t) for each parameter (Brooks and Gelman, 1998). The algorithm exhibits satisfactory convergence for all three chains, after a conservative 10000 iteration burn-in which is removed to compute the following now-casting and predictive results.

The temporal trend in the global time-varying reproduction number is shown in Figure 6, demonstrating marked variation through time either side of $R_t = 1$ as expected given the case timeseries trajectory in Figure 2. The credible intervals around R_t are narrow, reflecting the choice of case observation model and the large number of daily cases occurring in the UK as a whole, with variation due to spatial connectivity and risk accounted for by the model.

At the LAD-level, Figure 7 (left) shows the mean posterior local reproduction number R_{it} as of the 31st August 2021. Considerable spatial heterogeneity is seen, driven only in part by the spatial distribution of cases on the same date (Figure 2). This reflects the dynamics of the spatial epidemic over the whole time-window, with areas such as East Anglia exhibiting higher R_{it} values than might be concluded simply by looking at the most recent case data.

A convenient way to study the importance of spatial transmission is to plot the attributable fraction of the total infection risk on an individual in LAD i which is due to between-LAD transmission, defined as

$$AF_{it} = \frac{\phi \sum_{j \neq i} \frac{c_{ij} x_{jt}^1}{n_j}}{x_{it}^1 + \phi \sum_{j \neq i} \frac{c_{ij} x_{jt}^1}{n_j}}.$$

For a particular LAD of interest, the importance of spatial transmission therefore varies with both connectivity and within-LAD disease prevalence. For the most recent time-point in our case timeseries, we plot the posterior mean AF per LAD. Highly connected

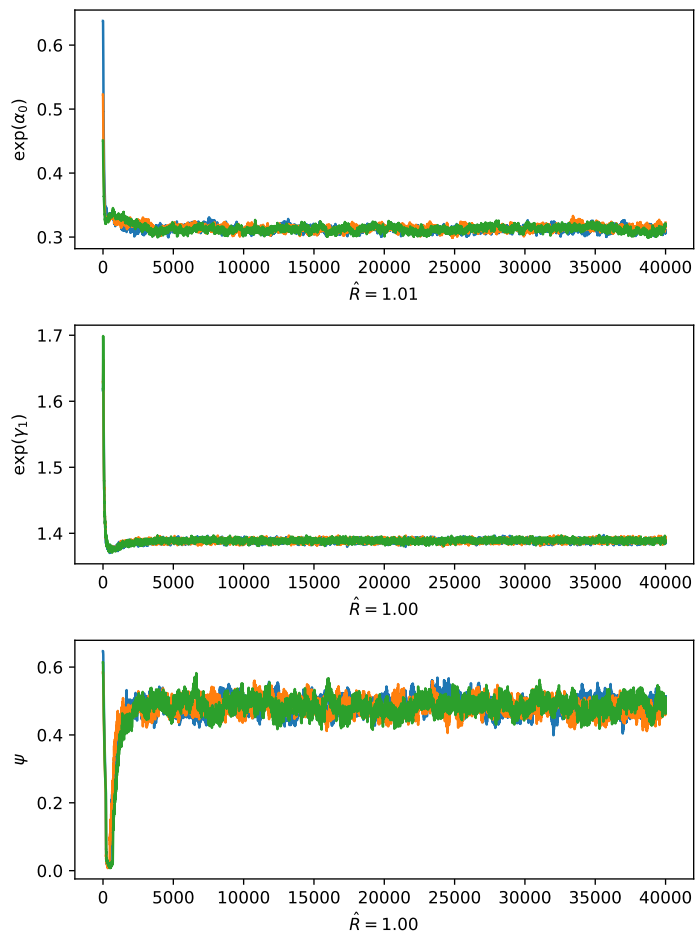


Fig. 5. Traceplots of uni-dimensional parameters $\exp(\alpha_0)$ (i.e. α_0 expressed as absolute infection risk per individual per day), $\exp(\gamma_1)$ (i.e. γ_1 expressed as relative risk), and ψ (infection rate per commute visit).

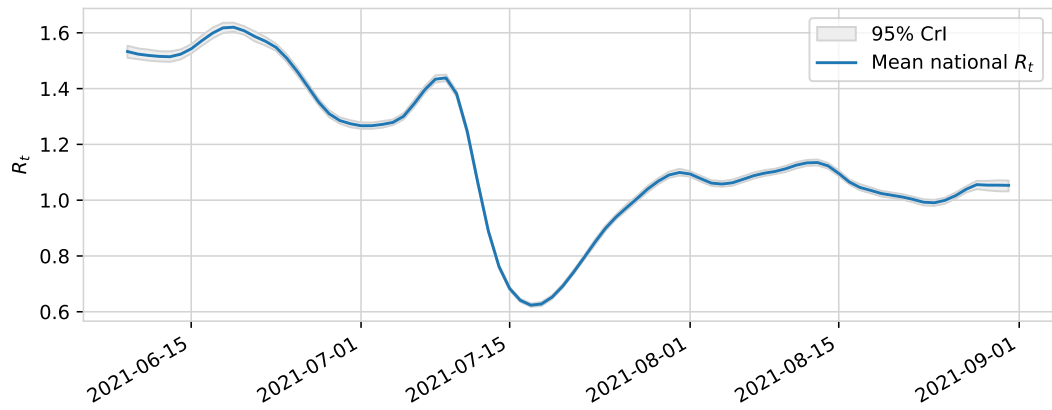


Fig. 6. Posterior distribution of R_t over the analysis period.

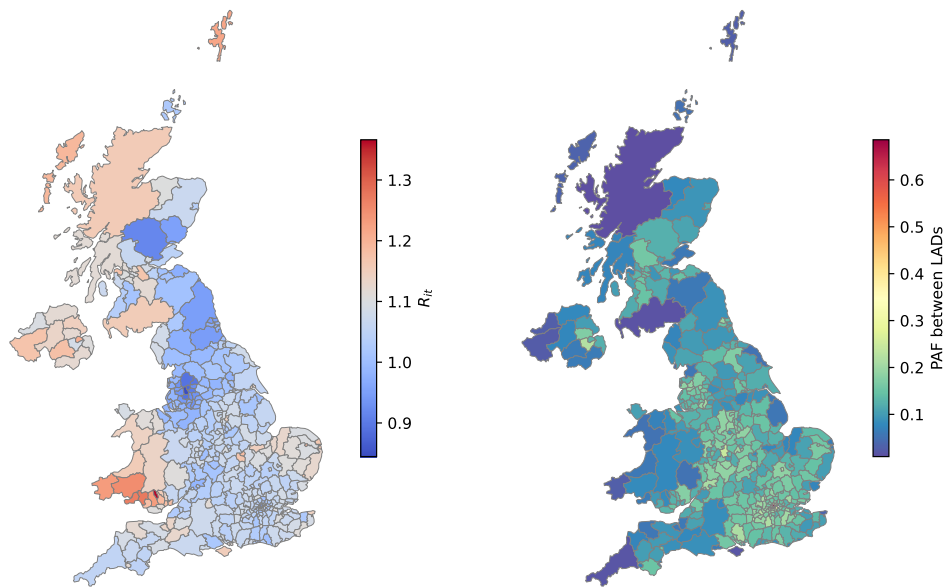


Fig. 7. Posterior mean spatial reproduction number R_{it} (left) and Population Attributable Fraction of the infection hazard due to between-LAD mobility (right) as of 31st August 2021.

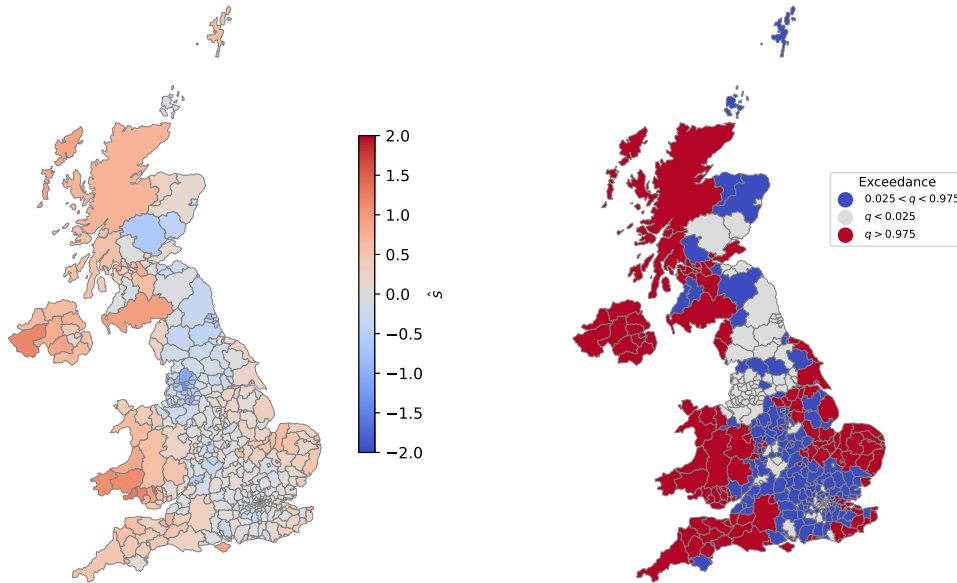


Fig. 8. Posterior mean of s (left), and exceedance probability $q = Pr(s > 0)$ (right) for each Local Authority District.

LADs, such as those comprising or close to the major cities, typically have a higher AF than more rural LADs, driven by overall population mobility.

Whilst our model captures the national-level baseline transmission rate and inter-LAD connectivity, it also allows local variation in baseline transmission rate through our spatially-correlated term s . The posterior mean of s and exceedance probability $Pr(s > 0)$ is plotted geographically in Figure 8. In general, these results indicate a trend towards higher baseline transmission in less densely populated, rural LADs compared to more populated, urban LADs.

Posterior predictive checking of our model was performed by comparing the 90% credible interval of the in-sample smoothing distribution of [IR] transitions against observed case numbers for the last two weeks of our analysis window. Out-of-sample checking was performed by comparing the 90% prediction interval of the 2-week-ahead predictive distribution against the subsequent 2 weeks' worth of case data. These comparisons are plotted for the Lancaster LAD in Figure 9. We see that our model captures both the modest increase and weekly periodicity of the case numbers well, accommodating the apparent “catch-up” in cases seen on a Monday after the propensity to test-and-report less at weekends. In practice, these plots are useful to detecting LADs departing from the expected epidemic trajectory early, so as to alert public health authorities to either case surges or unexpectedly low incidence in individual LADs.

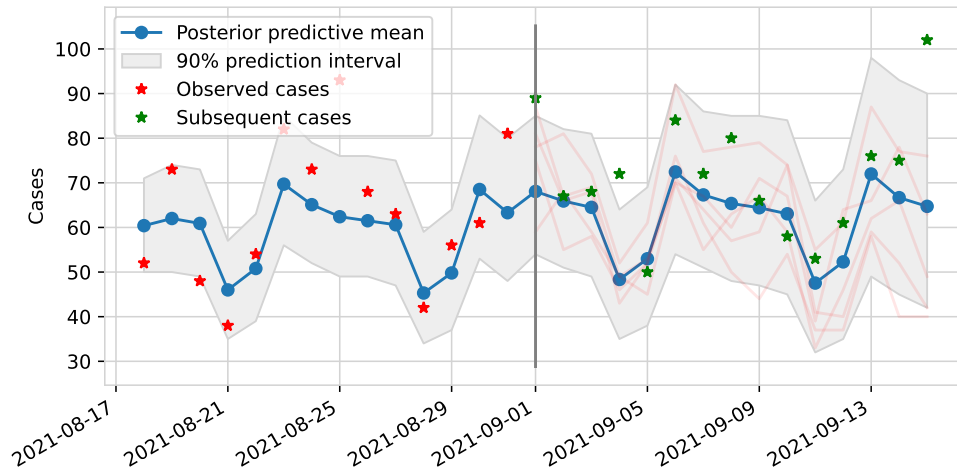


Fig. 9. Smoothing distribution (left of vertical line) and predictive distribution (right of vertical line) of number of [IR] events. The smoothing distribution is compared against the observed case data for the Lancaster LAD for the last 2 weeks of the analysis period, 18th June 2021 – 31st August 2021, whilst the predictive distribution is shown for a 2 week prediction horizon with subsequently observed cases superimposed.

6. Discussion

In this paper we have developed an MCMC-based method for fitting a discrete-time spatial stochastic SEIR model to geolocated case timeseries data for the COVID-19 pandemic in the UK. We address particularly the challenge of providing local now-casts and short-term forecasts of epidemic spread, based on knowledge of population structure and mobility. Our approach differs from “classic” epidemic models Birrell et al. (e.g. 2021), in that we make no attempt to fit our model to the entire epidemic timeseries (in the case of COVID-19 from the earliest cases in February 2020), but choose to analyse only the most recent 12 weeks of data. This reflects that the fact the epidemic in the UK was highly non-stationary, so that analysing a longer timeseries would likely have provided little further posterior information and run the risk of being misleading.

Our model represents a trade-off between its complexity and our ability to fit it to our 380-dimensional timeseries. It was implemented rapidly in response to the pandemic, with the innovation being the constrained-space samplers operating on the censored event data as in Section 3.1. To our knowledge, this is the first time that such an MCMC scheme has been attempted for a discrete-time model such as this.

As a principled fully Bayesian stochastic approach to the modelling and inference of spatio-temporal epidemics, the approach has many advantages. The MCMC algorithm works at scale, allowing the fitting of the COVID-19 model at the LAD level whilst incorporating human mobility in a pragmatic way; we remark that the approach is flexible enough to have been trivially extended to using dynamic mobility data, had it

been available. Importantly, the Bayesian treatment of censored transition event data allows our model to not only provide unbiased parameter inference, but also to provide probabilistic predictions of future case numbers with an improved measure of uncertainty consistent with all sources of modelled noise. Finally, the sole use of publicly available data and open source hardware/operating system-agnostic computational libraries aids portability and automation of the model. Indeed, during the COVID-19 pandemic, we deployed the model as an automatic nightly analysis pipeline requiring no manual intervention other than statistical oversight of the results. Despite the advantages of our approach, however, it is clear that further research is needed to address a number of key limitations as follows.

With individual-level epidemic models incorporating a high degree of population heterogeneity, it is common to attempt to estimate the baseline [IR] transition rate γ_0 (e.g. Jewell et al., 2009; McKinley et al., 2009; Chis Ster and Ferguson, 2007). However, it is known that estimating γ_0 in the presence of censored event times is problematic, requiring an exceptionally efficient sampler and re-parameterisation of the model to approximately orthogonalise γ_0 with respect to the censored data (Neal and Roberts, 2005). With interpretability of the parameters driving our model construction for this application, however, we chose to fix $\gamma_0 = \log 0.25$ based on clinically-derived data. This is a weak assumption compared to other modelling approaches (e.g. Scott et al., 2020), though it limits the capability to detect temporal changes in γ_0 which might occur as a result of improved case detection or changes in the host-pathogen interaction.

Our temporal and spatial random effects, α and \mathbf{s} respectively, were introduced following the observation that the disease transmission rate appeared to fluctuate across time and space more than could be explained by human mobility and the size of the population at risk. In principle, a spatiotemporal random effect could have been adopted, as is commonly used for disease mapping. However, such methods increase the dimensionality of the latent surface from $T + M$ to TM and typically require fast approximate methods to compute the posterior (Schrödle and Held, 2011; Zammit-Mangion et al., 2012). Even if such a method were to be applied to this model, the discrete nature of the censored event space would still require a Metropolis-Hastings approach such as ours, though an extremely efficient proposal would be required to ensure an adequate effective sample size.

A further pragmatic assumption adopted by our method is that the case timeseries is a perfect observation of the number of [IR] events per day. Though this assumption might hold incontrovertibly for highly pathogenic disease in small populations (such as foot-and-mouth disease in cattle), for large human populations in which social and demographic factors affect the propensity of an individual to take a test, a stochastic observation process would be preferable. Empirical testing showed that whilst our method could be implemented if the [IR] events were treated as latent – but informed by for example a Binomial model – the resulting algorithm was extremely slow to converge due to the extra censored data and the interactions within the epidemic event space this engendered.

The corollary to these limitations is that although our approach certainly has utility in informing disease control policy during an outbreak, the field of epidemic modelling is in urgent need of improved methods for inference in the presence of high-dimensional,

correlated, and discrete censored data. Whilst recent developments in particle filtering methods have offered promise for improving inference in individual-level models (e.g. (Ju et al., 2021; Rimella et al., 2023)), dependent stochastic metapopulation models such as ours still present a challenge for high-dimensional importance sampling. In MCMC methodology, recent advances in non-centering to orthogonalise state transition events with respect to the model parameters, these are based on individual-level continuous time models which fail to scale to national-level human population sizes (Pooley et al., 2015, 2019).

Finally, all modelling approaches are contingent on reliable and timely data to maximise their utility in prediction and policy advice. In this study, we based our analysis on publicly available case incidence data which as argued above is fraught with uncertainty due to changes in individuals’ preferences towards testing uptake. However, unbiased prevalence sampling data was collected in the UK during the pandemic, though was unavailable at the LAD-level due to concerns over data privacy (Eales et al., 2022; House et al., 2022). Nevertheless, the ability to use prevalence *as well as* incidence data for inference conditional on an epidemic model offers the possibility of improving parameter identifiability through observations not only of the 1st-order process (transitions), but also of the 0th-order process (epidemic compartments). Additionally, our approach would have been greatly improved with the addition of real-time human mobility data obtained indirectly through methods such as geolocation via cellular telephony. Such telephony data has been shown to be highly effective as a source of covariate data in epidemic models (Grantz et al., 2020). As it stands, our model is capable of explaining spatial patterns of disease spread via established commuting routes, but cannot separate spatially-homogeneous variation in human mobility due to social determinants (holiday periods, media announcements, etc) from the underlying transmissibility of the virus – the inclusion of accurate time-varying mobility data in place of our fixed commuting data would offer the opportunity to surmount this limitation. We therefore conclude by recommending that due consideration be made to appropriate sharing of these data during a future outbreak emergency, so that the full potential of spatial epidemic models be realised as a resource for policy information and evidence.

Competing interests

The authors declare no competing interests.

Acknowledgments

ACH and CPJ were supported through the Wellcome Trust ‘GEM: translational software for outbreak analysis’ (grant number UNS73114). ACH, CPJ, JR were supported by MRC through the JUNIPER modelling consortium (grant number MR/V038613/1). CPJ and GOR were supported by EPSRC (grant number EP/V042866/1).

We are indebted to the Google Research team, who helped us to implement our model, and fixed bugs in the underlying software libraries swiftly and effectively.

The authors would like to thank The High End Computing facility at Lancaster University for providing the facilities required for fitting the models in this paper.

The views expressed in this paper are those of the authors and not necessarily those of their respective funders or institutions.

Data availability

All data used in this analysis were public at the time of publication. COVID-19 case data is available from the UK Government Coronavirus website (Public Health England, 2020, 2021). Snapshots of the covariate data used for the analysis may be found in the accompanying software archive at <https://doi.org/10.5281/zenodo.7715657>.

References

- Abadi, M., Agarwal, A., Barham, P., Brevdo, E., Chen, Z., Citro, C., Corrado, G. S., Davis, A., Dean, J., Devin, M., Ghemawat, S., Goodfellow, I., Harp, A., Irving, G., Isard, M., Jia, Y., Jozefowicz, R., Kaiser, L., Kudlur, M., Levenberg, J., Mané, D., Monga, R., Moore, S., Murray, D., Olah, C., Schuster, M., Shlens, J., Steiner, B., Sutskever, I., Talwar, K., Tucker, P., Vanhoucke, V., Vasudevan, V., Viégas, F., Vinyals, O., Warden, P., Wattenberg, M., Wicke, M., Yu, Y. and Zheng, X. (2015) TensorFlow: Large-scale machine learning on heterogeneous systems. URL: <https://www.tensorflow.org/>. Software available from tensorflow.org.
- Bartlett, M. S. (1964) The relevance of stochastic models for large-scale epidemiological phenomena. *Journal of the Royal Statistical Society: Series C (Applied Statistics)*, **13**, 2–8. URL: <https://rss.onlinelibrary.wiley.com/doi/abs/10.2307/2985217>.
- Becker, N. (1981) A general chain binomial model for infectious diseases. *Biometrics*, 251–258.
- Birrell, P., Blake, J., van Leeuwen, E., Gent, N. and De Angelis, D. (2021) Real-time nowcasting and forecasting of COVID-19 dynamics in England: the first wave. *Phil. Trans. R. Soc. B*, **376**, 20200279.
- Brand, S., Tildesley, M. J. and Keeling, M. J. (2015) Rapid simulation of spatial epidemics : a spectral method. *Journal of Theoretical Biology*, **Volume 370**, 121–134. URL: <https://wrap.warwick.ac.uk/67531/>.
- Brooks, S. and Gelman, A. (1998) General methods for monitoring convergence of iterative simulations. *Journal of Computational and Graphical Statistics*, **7**, 434–455.
- Carpenter, B., Gelman, A., Hoffman, M. D., Lee, D., Goodrich, B., Betancourt, M., Brubaker, M., Guo, J., Li, P. and Riddell, A. (2017) Stan: A probabilistic programming language. *Journal of Statistical Software, Articles*, **76**, 1–32. URL: <https://www.jstatsoft.org/v076/i01>.
- Chapman, L., Jewell, C., Spencer, S., Pellis, L., Datta, S., Chowdhury, R., Bern, C., Medley, G. and Hollingsworth, T. (2018) The role of case proximity in transmission of visceral leishmaniasis in a highly endemic village in Bangladesh. *PLOS Neglected Tropical Diseases*, **12**, 1–29. URL: <https://doi.org/10.1371/journal.pntd.0006453>.

- Chis Ster, I. and Ferguson, N. M. (2007) Transmission Parameters of the 2001 Foot and Mouth Epidemic in Great Britain. *PLOS ONE*, **2**, 1–12. URL: <https://doi.org/10.1371/journal.pone.0000502>.
- Deardon, R., Brooks, S., Grenfell, B., Keeling, M., Tildesley, M., Savill, N., Shaw, D. and Woolhouse, M. (2010) Inference for individual-level models of infectious diseases in large populations. *Statistica Sinica*, **20**, 239–261.
- Diekmann, O., Othmer, H., Planqué, R., and Bootsma, M. (2021) The discrete-time Kermack–McKendrick model: A versatile and computationally attractive framework for modeling epidemics. *Proc. Nat. Acad. Sci.*, **18**, e2106332118.
- Dillon, J. V., Langmore, I., Tran, D., Brevdo, E., Vasudevan, S., Moore, D., Patton, B., Alemi, A., Hoffman, M. D. and Saurous, R. A. (2017) Tensorflow distributions. *CoRR*, [abs/1711.10604](https://arxiv.org/abs/1711.10604). URL: <http://arxiv.org/abs/1711.10604>.
- Eales, O., Wang, H., Haw, D., Ainslie, K. E. C., Walters, C. E., Atchison, C., Cooke, G., Barclay, W., Ward, H., Darzi, A., Ashby, D., Donnelly, C. A., Elliott, P. and Riley, S. (2022) Trends in SARS-CoV-2 infection prevalence during England’s roadmap out of lockdown, January to July 2021. *PLOS Computational Biology*, **18**, 1–16. URL: <https://doi.org/10.1371/journal.pcbi.1010724>.
- Grantz, K., Meredith, H., Cummings, D., Metcalf, C., Grenfell, B., Giles, J., Mehta, S., Solomon, S., Labrique, A., Kishore, N., Buckee, C. and Wesolowski, A. (2020) The use of mobile phone data to inform analysis of COVID-19 pandemic epidemiology. *Nature Communications*, **11**, 4961.
- Grenfell, B. T., Bjørnstad, O. N. and Finkenstädt, B. F. (2002) Dynamics of Measles Epidemics: Scaling Noise, Determinism, and Predictability with the TSIR Model. *Ecological Monographs*, **72**, 185–202. URL: <http://www.jstor.org/stable/3100024>.
- House, T., Riley, H., Pellis, L., Pouwels, K. B., Bacon, S., Eidukas, A., Jahanshahi, K., Eggo, R. M. and Walker, A. S. (2022) Inferring risks of coronavirus transmission from community household data. *Statistical Methods in Medical Research*, **31**, 1738–1756. URL: <https://doi.org/10.1177/09622802211055853>. PMID: 36112916.
- Jewell, C., Kypraios, T., Neal, P. and Roberts, G. (2009) Bayesian analysis for emerging infectious diseases. *Bayes. Anal.*, **4**, 465–496.
- Ju, N., Heng, J. and Jacob, P. E. (2021) Sequential Monte Carlo algorithms for agent-based models of disease transmission.
- Keeling, M. J. and Eames, K. T. (2005) Networks and epidemic models. *J. R. Soc. Interface*, **2**, 295–307.
- Keeling, M. J., Woolhouse, M. E. J., Shaw, D. J., Matthews, L., Chase-Topping, M., Haydon, D. T., Cornell, S. J., Kappey, J., Wilesmith, J. and Grenfell, B. T. (2001) Dynamics of the 2001 UK Foot and Mouth Epidemic: Stochastic Dispersal in a Heterogeneous Landscape. *Science*, **294**, 813–817. URL: <https://www.science.org/doi/abs/10.1126/science.1065973>.

- Levins, R. (1969) Some demographic and genetic consequences of environmental heterogeneity for biological control. *Bulletin of the Entomological Society of America*, **15**, 237–240.
- Lipshtat, A., Alimi, R. and Ben-Horin, Y. (2021) Commuting in metapopulation epidemic modeling. *Scientific Reports*, **11**, 15198. URL: <https://doi.org/10.1038/s41598-021-94672-w>.
- McKinley, T., Cook, A. R. and Deardon, R. (2009) Inference in epidemic models without likelihoods. *The International Journal of Biostatistics*, **5**. URL: <https://doi.org/10.2202/1557-4679.1171>.
- Minh, P., Stevenson, M., Jewell, C., French, N. and Schauer, B. (2011) Spatio-temporal analyses of highly pathogenic avian influenza H5N1 outbreaks in the Mekong River Delta, Vietnam, 2009. *Spatial and Spatio-temporal Epidemiology*, **2**, 49–57. URL: <https://www.sciencedirect.com/science/article/pii/S1877584510000572>.
- Neal, P. and Roberts, G. (2005) A case study in non-centering for data augmentation: Stochastic epidemics. *Statistics and Computing*, **15**, 315–327.
- Neal, P. J. and Roberts, G. O. (2004) Statistical inference and model selection for the 1861 Hagelloch measles epidemic. *Biostatistics*, **5**, 249–261.
- Palomo-Briones, G., Siller, M. and Grignard, A. (2022) An agent-based model of the dual causality between individual and collective behaviors in an epidemic. *Comput Biol Med*, **141**, 104995.
- Pooley, C., Bishop, S., Doeschl-Wilson, A. and Marion, G. (2019) Posterior-based proposals for speeding up Markov chain Monte Carlo. *Royal Society Open Science*, **6**, 190619.
- Pooley, C., Bishop, S. and Marion, G. (2015) Using model-based proposals for fast parameter inference on discrete state space, continuous-time Markov processes. *J. R. Soc. Interface*, **12**, 20150225.
- Probert, W. J. M., Jewell, C. P., Werkman, M., Fonnesebeck, C. J., Goto, Y., Runge, M. C., Sekiguchi, S., Shea, K., Keeling, M. J., Ferrari, M. J. and Tildesley, M. J. (2018) Real-time decision-making during emergency disease outbreaks. *PLOS Computational Biology*, **14**, 1–18. URL: <https://doi.org/10.1371/journal.pcbi.1006202>.
- Public Health England (2020) GOV.UK Coronavirus (COVID-19) in the UK. <https://coronavirus.data.gov.uk>. Accessed: 2021-06-15.
- (2021) UK LAD-level new cases by specimen date. <https://api.coronavirus.data.gov.uk/v2/data?areaType=ltla&metric=newCasesBySpecimenDate&format=csv&release=2021-06-15>. Accessed: 2021-06-15.
- Quesada, J., López-Pineda, A., Gil-Guillén, V., Arriero-Marín, J., Gutiérrez, F. and Carratala-Munuera, C. (2021) Incubation period of COVID-19: A systematic review and meta-analysis. *Revista Clínica Española (English Edition)*, **221**, 109–117. URL: <https://www.sciencedirect.com/science/article/pii/S2254887420301466>.

- Rimella, L., Jewell, C. and P, F. (2023) Approximating Optimal SMC Proposal Distributions in Individual-Based Epidemic Models. *Statistica Sinica*. In press.
- Schrödle, B. and Held, L. (2011) Spatio-temporal disease mapping using INLA. *Environmetrics*, **22**, 725–734. URL: <https://onlinelibrary.wiley.com/doi/abs/10.1002/env.1065>.
- Scott, J. A., Gandy, A., Mishra, S., Unwin, J., Flaxman, S. and Bhatt, S. (2020) *epidemia: Modeling of Epidemics using Hierarchical Bayesian Models*. URL: <https://imperialcollegelondon.github.io/epidemia/>. R package version 1.0.0.
- Sellman, S., Tsao, K., Tildesley, M. J., Brommesson, P., Webb, C. T., Wennergren, U., Keeling, M. J. and Lindström, T. (2018) Need for speed : an optimized gridding approach for spatially explicit disease simulations. *PLOS Computational Biology*, **14**.
- Smieszek, T., Balmer, M., Hattendorf, J., Axhausen, K., Zinsstag, J. and Scholz, R. (2011) Reconstructing the 2003/2004 H3N2 influenza epidemic in Switzerland with a spatially explicit, individual-based model. *BMC infectious diseases*, **11**, 115.
- Swallow, B., Birrell, P., Blake, J., Burgman, M., Challenor, P., Coffeng, L. E., Dawid, P., De Angelis, D., Goldstein, M., Hemming, V., Marion, G., McKinley, T. J., Overton, C. E., Panovska-Griffiths, J., Pellis, L., Probert, W., Shea, K., Villela, D. and Vernon, I. (2022) Challenges in estimation, uncertainty quantification and elicitation for pandemic modelling. *Epidemics*, **38**, 100547. URL: <https://www.sciencedirect.com/science/article/pii/S1755436522000093>.
- Tian, S., Hu, N., Lou, J., Chen, K., Kang, X., Z, X., H, C., Wang, D., Liu, N., Liu, D., Chen, G., Zhang, Y., Li, D., Li, J., Lian, H., Niu, S., Zhang, L. and Zhang, J. (2020) Characteristics of COVID-19 infection in Beijing. *Journal of Infection*, **80**, 401–406. URL: <https://www.sciencedirect.com/science/article/pii/S0163445320301018>.
- Tildesley, M., Savill, N., Shaw, D., Deardon, R., Brooks, S., Woolhouse, M., Grenfell, B. and Keeling, M. (2006) Optimal reactive vaccination strategies for a foot-and-mouth outbreak in the UK. *Nature*, **440**, 83–86.
- Zammit-Mangion, A., Sanguinetti, G. and Kadiramanathan, V. (2012) Variational estimation in spatiotemporal systems from continuous and point-process observations. *IEEE Transactions on Signal Processing*, **60**, 3449–3459.